Microscopic insights on field induced switching and domain wall motion in orthorhombic ferroelectrics

Ruben Khachaturyan [1], Yijing Yang [1,2], Sheng-Han Teng [1,3], Benjamin Udofia [1], Markus Stricker [1], and Anna Grünebohm [1,3,*]

[1]*Interdisciplinary Centre for Advanced Materials Simulation (ICAMS), Ruhr-University Bochum, Universitätsstrasse 150, 44801 Bochum, Germany*

[2]*Université Paris-Saclay, Université Evry, CY Cergy Paris Université, CNRS, LAMBE, 91025, Evry-Courcouronnes, France*

[3]*Center for Interface-Dominated High Performance Materials (ZGH), Ruhr-University Bochum, Universitätsstrasse 150, 44801 Bochum, Germany*

Surprisingly little is known about the microscopic processes that govern ferroelectric switching in orthorhombic ferroelectrics. To study these processes, we combine *ab initio*-based molecular dynamics simulations and data science on the prototypical material $BaTiO_3$. We reveal two different field regimes: For moderate field strengths, the switching is dominated by domain wall motion, while a fast bulklike switching can be induced for large fields. Switching in both field regimes follows a multistep process via polarization directions perpendicular to the applied field. In the former case, the moving wall is of Bloch character and hosts dipole vortices due to nucleation, growth, and crossing of two-dimensional 90° domains. In the second case, the local polarization shows a continuous correlated rotation via an intermediate tetragonal multidomain state.

I. INTRODUCTION

It is an open question whether the reversal of polarization in ferroelectrics happens mainly by direct switching by 180° or in successive multistep events, e.g., two 90° steps. In macroscopic models, the energy barrier for direct switching is larger than for successive switching events [1–5]. The latter has also been reported for single crystals [6–8] and polycrystalline samples [9,10]. Furthermore, it has been discussed that correlated and coherent multistep switching, e.g., by preexisting domain structures, cannot be distinguished from direct switching on the macroscopic scale [2,3]. However, it is also known that homogeneous switching is only relevant for high field strengths and defect-free materials [11]. Otherwise, switching is related to nucleation at interfaces or defects and the consecutive growth of nuclei [12–19]. The realization of multistep switching by nucleation and growth is thus challenged by electrostatic and elastic interface energies.

Ferroelectric domain walls (DWs) are the interfaces between regions with different polarizations (P). It is settled that the characteristics of ferroelectric switching and polarization kinetics depend on DWs and their dynamics. However, the underlying microscopic processes are not fully clear and even the nature of the polarization change across walls is again under debate [14,20]. On charge-neutral walls, the component of the polarization vector parallel to the wall ($P_{||}$) switches its sign. For a long time, it was accepted that this switching is Ising-like with a local reduction of the magnitude of P; see Fig. 1(a) [21,22]. However, phenomenological models

have predicted that (meta-)stable Bloch-like DWs with the rotation of the order parameter on the wall, i.e., a finite P_t [see Fig. 1(b)], may exist in orthorhombic [23,24] and rhombohedral ferroelectric phases [24–28]. Bloch walls with locally varying rotation direction and Neél walls with finite polarization perpendicular to the wall have been reported [25,29]. For tetragonal ferroelectrics, Bloch-like walls have been discussed for $PbTiO_3$ [30,31] and for particular wall directions in Pb-free materials [32–34]. As reviewed by Cherifi-Hertel [29], there is experimental evidence on non-Ising walls. However, Bloch walls are less common than in theoretical predictions, which may be partly related to the surface sensitivity of the experimental analysis [35–38]. On the other hand, most theoretical predictions are sensitive to the chosen parametrization and may overestimate the polarization rotation.

Microscopic theoretical studies on ferroelectric switching and domain wall motion allow for the fundamental understanding of the underlying nucleation processes and have been successfully used to predict the acceleration of the switching by nonequilibrium effects [11,15,16,39,40] as well as complex multistep switching by twinning for 90° walls [41]. However, the existing literature mostly focuses on tetragonal ferroelectrics, while orthorhombic phases are also common around room temperature, e.g., in $(K, Na)NbO_3$ and solid solutions based on $BaTiO_3$. In one of the few microscopic studies, macroscopic multistep switching has been reported for $BaTiO_3$ in noncollinear electrical fields [42].

In this paper, we combine microscopic simulations with methods from data science to study field induced polarization switching and domain wall dynamics of the orthorhombic phase of $BaTiO_3$. We find two switching scenarios: For moderate fields, the polarization switches by field induced motion
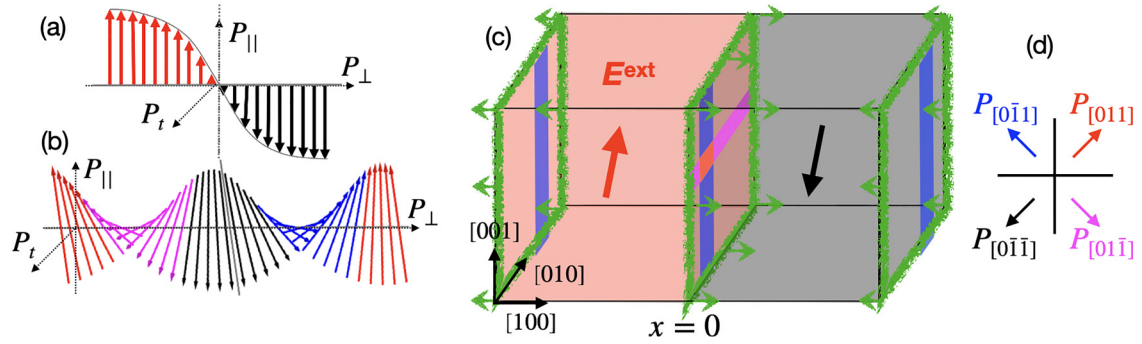
---
*anna.gruenebohm@rub.de

FIG. 1. Idealized Ising and Bloch walls with 180° switching of the polarization via (a) $|P| = 0$ ($P_\perp = P_t = 0$) and (b) the rotation of the polarization via $\pm P_t$ ($P_\perp = 0$, $|P| = $ const). (c) Illustration of our simulation setup. Initially, the system is in the orthorhombic phase with 180° domain walls normal to [100] (green frames), a simulation cell of $144 \times 48 \times 48$ f.u. in combination with periodic boundary conditions is used, and the discussion focuses on the wall initially centered at $x = 0$. Thereby, each formula unit (f.u.) contains one BaTiO$_3$ unit. The local polarization in both domains points along $P_{||} = \pm P_{[011]}$, while the components $P_\perp = \pm P_{[100]}$ and $P_t = \pm P_{[01\bar{1}]}$ are zero. (d) Color encoding: We classify the dipoles by the signs of their [011] components as black ($--$), red ($++$), blue ($-+$), and magenta ($+-$). After a field is applied along [011] ($\boldsymbol{E}^{\mathrm{ext}}$), the parallel domain (red) grows and the walls move (green arrows).

of DWs via two-dimensional nucleation and growth. Excitingly, this is related to a multistep nucleation and growth process, Bloch-like polarization rotation, and polarization vortices. For high fields, the polarization switches via an ultrafast, homogeneous switching path which starts in the center of the domains and propagates in all directions in three-dimensional space.

II. METHODS

We use molecular dynamics (MD) to simulate the field-driven evolution of the polarization vector field. Concretely, we use the effective Hamiltonian by Zhong *et al.* [43] parametrized by *ab initio* simulations [44] and the FERAM code [45]. This approach allows one to efficiently model the microscopic properties of ferroelectrics as the collective atomic displacements are coarse grained to the most relevant degrees of freedom per BaTiO$_3$ formula unit (f.u.): the acoustic displacement vector $\boldsymbol{w}$ and the soft mode vector $\boldsymbol{u}$ which corresponds to the local dipole moment $\boldsymbol{p} = Z^* \boldsymbol{u}$, with Z^* the effective Born charge. The Hamiltonian is given as

$$
\begin{aligned}
H^{\mathrm{eff}} &= V^{\mathrm{self}}(\{\boldsymbol{u}\}) + V^{\mathrm{dpl}}(\{\boldsymbol{u}\}) + V^{\mathrm{short}}(\{\boldsymbol{u}\}) \\
&+ V^{\mathrm{elas}}(\eta_1, \ldots, \eta_6, \{\boldsymbol{w}\}) \\
&+ V^{\mathrm{coup}}(\{\boldsymbol{u}\}, \{\boldsymbol{w}\}, \eta_1, \ldots, \eta_6) \\
&- Z^* \sum_i \boldsymbol{E}^{\mathrm{ext}} \cdot \boldsymbol{u}_i + \frac{M^*_{\mathrm{dipole}}}{2} \sum_{i,\alpha} \dot{\boldsymbol{u}}^2_{\alpha,i},
\end{aligned}
\tag{1}
$$

where $V^{\mathrm{self}}(\{\boldsymbol{u}\})$, $V^{\mathrm{dpl}}(\{\boldsymbol{u}\})$, and $V^{\mathrm{short}}(\{\boldsymbol{u}\})$ are the self-energy, the long-range dipole-dipole interaction, and the short-range interactions of the local soft modes. The elastic energy V^{elas} depends on $\{\boldsymbol{w}\}$ and the homogeneous strain tensor η_i given in Voigt notation and V^{coup} includes the couplings between the local soft mode and strain. The last two terms represent the coupling to the external field $\boldsymbol{E}^{\mathrm{ext}}$ and the kinetic energy of the local mode, with M^*_{dipole} being the effective mass of the soft mode. The strain is internally optimized during each MD step. Previous work demonstrated

the high predictive power of this method for DWs and their dynamics [39,46,47].

Figure 1(c) is a sketch of our simulation setup. Without loss of generality, we study the orthorhombic phase with polarization along $\pm[011]$ and an external field ($\boldsymbol{E}^{\mathrm{ext}}$) applied along [011] and focus on typical 180° walls with $\langle 100 \rangle$ normal (O180) [24,48]. We use a system size of $144 \times 48 \times 48$ f.u. together with periodic boundary conditions and initialize a periodic array of 180° DWs in x planes. For the DW distances of 28 nm, interactions between neighboring walls are negligible [16,49]. Furthermore, finite-size effects and thermal noise are small and we validate our results by independent simulation with different random initialization of dipoles.

We apply the field protocol from Ref. [39] to equilibrate the system in this well-defined domain structure, i.e., we randomly initialize local dipoles while applying local external fields and thermalize the system in the orthorhombic phase (40 K apart from the tetragonal to orthorhombic (T-O) transition temperatures found for cooling by our model) using the Nosé-Poincaré thermostat [50]. These fields are removed and, after further equilibration, $\boldsymbol{E}^{\mathrm{ext}}$ is applied instantaneously, and we analyze the time evolution of the polarization vector field on slices parallel to the wall ($\langle p_z \rangle_x$), i.e., on layers x; see Fig. 1(c).[1] We track the evolution of the domain wall width (d_{DW}) and the velocity of the domain wall center ($v_{\mathrm{DW}} = \dot{x}_0$) by fitting the mean polarization per layer at each time step via [39]

$$
\langle p_z \rangle_x = p_0 \tanh\left[\frac{x - x_0}{d_{\mathrm{DW}}}\right] + \varepsilon,
\tag{2}
$$

where the fitting parameters p_0 and ε correspond to the saturation polarization without an external field and time-dependent corrections, respectively.[2] Complementarily, we estimate v_{DW}

---

[1]Note that the multistep switching on the moving walls was also reproduced applying the field with a ramping rate 1 kV/mm per picosecond.

[2]Note that the converse piezoelectric effect results in a time-dependent increase of polarization with domain wall motion.

in the steady state based on the macroscopic change of polarization ΔP as

$$v_{\text{DW}} = \frac{a_0 L_x}{2} \frac{\Delta P(E)}{t} \frac{1}{p_{\text{DW}}}, \tag{3}$$

where p_{DW}, a_0, and L_x are the polarization gain by switching one unit cell, the lattice constant, and the number of unit cells in the x direction, respectively, and the presence of two walls in the system is accounted for by the factor of $1/2$. We estimate p_{DW} by the difference between the mean polarization in both domains 30 ps after the field has been applied. In both cases, v_{DW} is averaged over four independent simulations in the time interval 30–60 ps.

We analyze the formation of polarization vortices on the moving wall by integrating the winding angle $\Delta\phi_i = \arccos \frac{u_{i+1} \cdot u_i}{|u_{i+1}||u_i|}$ enclosed between neighboring dipoles along the closed loop in a counterclockwise direction on all lattice positions [51],

$$\Phi_i = \frac{1}{2\pi} \sum_{i=1}^{4} \Delta\phi_i.$$

We furthermore analyze the time evolution of the distribution of local dipoles p_i and clusters of dipoles. This analysis is done on separate x planes (slices). We classify the local dipoles by the sign of their [011] components [see Fig. 1(d)]:

red: $p_z > 0 \wedge p_y > 0$ ($P_{||}$, parallel to E^{ext}),
black: $p_z < 0 \wedge p_y < 0$ ($P_{||}$, antiparallel to E^{ext}),
magenta: $p_z > 0 \wedge p_y < 0$ (P_t, perpendicular to E^{ext}),
blue: $p_z < 0 \wedge p_y > 0$ (P_t, perpendicular to E^{ext}),

and define a cluster as a connected region of unit cells (cross-shaped stencil) within the same class on one plane. The presented statistics and averages are taken across the evolution of all clusters and times.[3] The cluster analysis is realized through a wrapper around the labeling capabilities as implemented in the `skicit-image` library [52].

Note that thermal fluctuations cannot be clearly separated from the initial nuclei formation. To exclude the former, we start with 10 independent simulations per field strength over the time interval 3–100 ps and filter out all cluster sizes which exist for one time step (1 ps) only. We further exclude the final cluster, i.e., the fully switched slice. Our data set then consists of the time evolution of all slices of all 10 simulations. Based on cluster area histograms of vanishing clusters, we extract a critical area by fitting an exponential. The critical area is then extracted as the intersection of this exponential with occurrence frequency "1." This is what we define as the critical area because it is the upper bound for unstable clusters. At the same time, this value is a good approximation of the lower bound for the critical nucleus area or extent. For all clusters which grow at least as large as these values, we subsequently assess the time evolution of their extent and area at the critical cluster size using a quadratic fit. All scripts used for the analysis are available on our git repository [53].

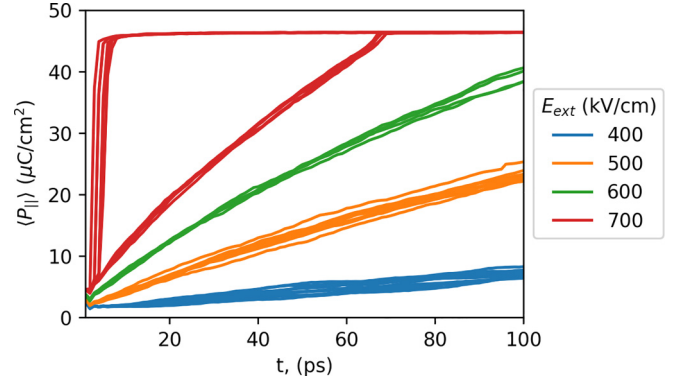
[3]Diagonally connected cells are not counted as neighbors.

FIG. 2. Time evolution of the macroscopic polarization component $P_{||}$ after external fields of 400 kV/cm (blue), 500 kV/cm (orange), 600 kV/cm (green), and 700 kV/cm (red) have been applied to independent initial states. Initially, the system is in the bidomain state with equal domain width ($P_{||} = 0$). For 700 kV/cm, about 8 of 10 simulations follow the fast switching scenario discussed in Sec. III C.

III. RESULTS

We start our analysis with a systematic screening of different field strengths. One can distinguish three switching regimes (see Fig. 2):

(I) Below 400 kV/cm, the change of polarization with time is minor (not shown).

(II) Above this field strength, the polarization increases with time until the saturation polarization of the single-domain state in the external field is reached. Thereby, the velocity of switching is initially accelerated and a steady state with approximate linear $P(t)$ is reached after about 30 ps. The speed of the DWs increases with increasing field strength. This switching by wall motion is discussed in Sec. III A.

(III) For 700 kV/cm, the system already switches to the single-domain state before the steady state is reached in about 8 of 10 simulations. This bulklike switching is discussed in Sec. III C.

Both the activation field for wall motion and the increase of the switching velocity with the field strength are well known for ferroelectric switching [20]. Furthermore, the initial acceleration of the walls [39] and the bulklike switching for high fields [11] have been reported for tetragonal BaTiO$_3$. However, as discussed in the following, the underlying microscopic processes differ considerably between tetragonal (T) and orthorhombic (O) phases.

A. Field induced domain wall motion

What are the underlying microscopic processes in the switching regime (II)? The switching process is dominated by wall motion as the velocities of the walls estimated from the macroscopic polarization change by Eq. (3), i.e., from the superposition of DW motion and other changes of the polarization, is only about 6% larger compared to the actual speed [Eq. (2), added in brackets] with 75 ± 4 (71 ± 6), 126 ± 8 (117 ± 11), and 183 ± 3 m/s (172 ± 4 m/s) for 500, 600, and 700 kV/cm.

As discussed in the literature for the tetragonal phase [15,16,39], thermal fluctuations of local dipoles increase on
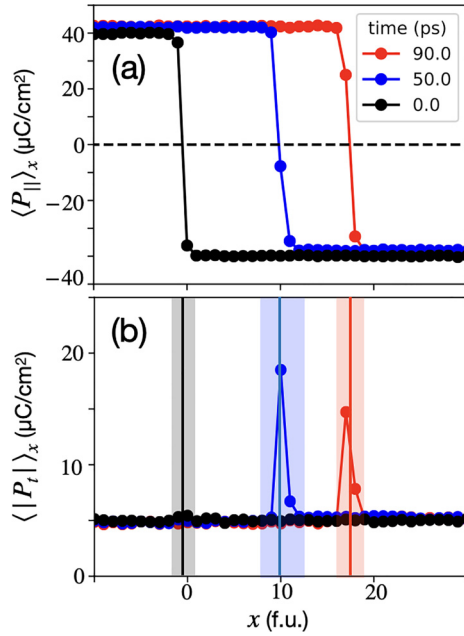
FIG. 3. Polarization profile across an O180 domain wall (0 ps, black), 50 ps (blue), and 90 ps (red) after an external field of $E^{ext} = 500$ kV/cm has been applied. (a) $P_\parallel$, the polarization projected on the field direction [011]; (b) P_t, the polarization projected on [0$\bar{1}$1]. Note that for P_t, the sign of the projection has been removed before averaging. Vertical lines and shaded areas highlight the center and the width of the domain wall at the corresponding time steps.

DWs due to frustrated interactions, reduced polarization, and shallower energy minima. In addition, the critical field strength for the onset of switching is locally reduced. Figure 3 shows the polarization profile across the initial domain structure (black) and 50 ps (blue) and 90 ps (red) after the application of 500 kV/cm. Initially, the walls are sharp with a width of about 1 f.u., and we can reproduce the prediction by Landau theory [24], which states that the equilibrium wall configuration is of Ising type, i.e., P_t and $P_\perp$ at the wall cannot be distinguished from thermal noise. In steady-state motion, the mean wall width increases to 1.2 f.u. (±10%). Excitingly, the applied field changes the character of the walls to mixed Ising-Bloch-like with $\langle|P_t|\rangle \approx 20$ μC/cm^2; see Fig. 3(b). On the other hand, no Néel-like polarization rotation is induced as $P_\perp$ changes neither globally nor locally; cf. Fig. 11. Exemplarily, Fig. 4 shows the time evolution of the dipole distribution on a slice parallel to the domain wall for 500 kV/cm. Initially, the dipoles are in the metastable black state antiparallel to the applied field and all dipoles scatter around the mean value of polarization of about $P_\parallel = -37$ μC/cm^2; see Figs. 4(a) and 4(d). After full switching (not shown), the dipoles analogously scatter around the mean value of the red state of about $P_\parallel = 43$ μC/cm^2, which is the energetic ground state in the applied field. During switching, the dipoles have to cross the energy barriers between these two states. As the probability for the realization of a particular point in configuration space depends on its energy [54], Figs. 4(a)–4(c) allow us to draw important conclusions on the switching process: On the one hand, no dipoles are present in the center of the $p_{[001]} - p_{[010]}$ plane for all times. The barrier corresponding to direct 180°
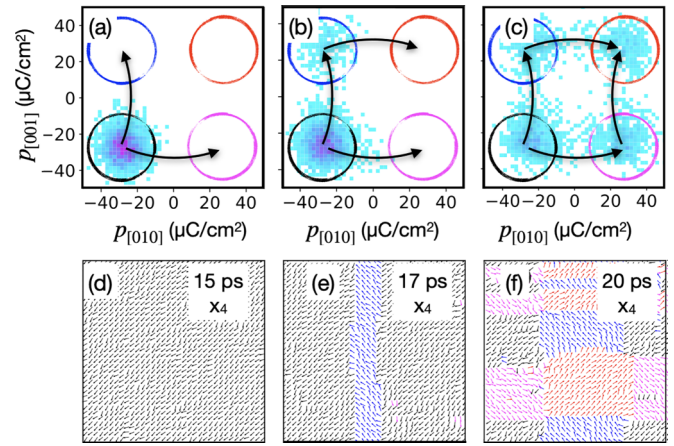

FIG. 4. Time evolution of the dipole distribution in slice x_4 (a)–(c) in $p_{[010]} - p_{[001]}$ space and (d)–(f) in real space after 500 kV/cm have been applied along the red direction. Colors encode (a)–(c) the number of dipoles per $(2.06$ μC/cm$^2)^2$ area and (d)–(f) the dipole direction. Black arrows show the proposed transition path. (a),(d) 15 ps (distance to DW center: 1.6 f.u.); (b),(e) 17 ps (distance to DW center: 1.1 f.u.); and (c),(f) 20 ps (distance to DW center: 0.1 f.u.).

switching is thus too high for the given field strength and temperature. On the other hand, the $\langle 100 \rangle$-type directions are lower in energy and are populated at intermediate times. For the shown example, a fraction of dipoles already crossed one of these barriers at 17 ps and has entered the blue state, i.e., the local energy minimum with $P_{[010]} > 0$ and $|P_{[010]}| \approx |P_{[001]}|$ with polarization perpendicular to the applied field. Consequently, the two-step 90° switching across the $\langle 100 \rangle$-type directions is not only lower in energy than direct switching in homogeneous phenomenological models [55], but also on the microscopic scale.

It is important to note that the macroscopic polarization does not switch in two discrete steps in time. For all times, a variety of intermediate angles of polarization is present. This multistage switching is activated by thermal fluctuations of local dipoles, but does not occur homogeneously in space. This can be understood by the polarization gradient and the bound charges $\rho = -(\partial P_i / \partial x_i)$ related to a depolarization field and an energy penalty [15] proportional to ρ^2 induced if locally the sign of the polarization component i switches relative to its surrounding. Therefore, the z and y interfaces of blue and magenta and all interfaces of red clusters with the black matrix are high in energy, respectively. The switching happens by nucleation and growth of local clusters; see Figs. 4(e) and 4(f). Analogous to the discussion on tetragonal domain walls in Refs. [15,54], the shape and interface of the nuclei deviates from classical nucleation theory by Miller-Weinreich [18,19] and we find approximately rectangular nuclei with diffuse interfaces.

As discussed in Sec. II, the initial nucleation and thermal fluctuations are not easy to distinguish and we thus define disappearing and persisting clusters as approximate measures. Thereby, it is convenient to distinguish between the initial switching to blue and magenta directions and the final switching to the red direction. For 400 kV/cm, the number of disappearing clusters is more than five times larger for
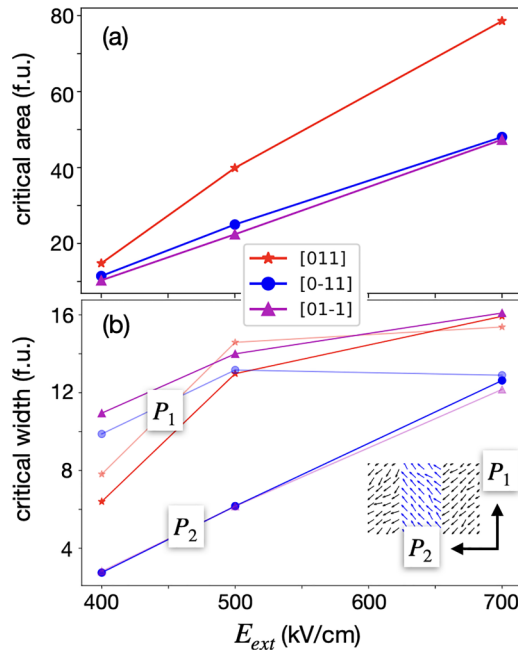
FIG. 5. Change of critical cluster (a) area and (b) width for blue, magenta, and red clusters as a function of field strength. In (b), one can distinguish the critical width for the direction without (P_1) and with (P_2) reversal of the sign of the polarization component, as illustrated in the inset for the blue cluster.
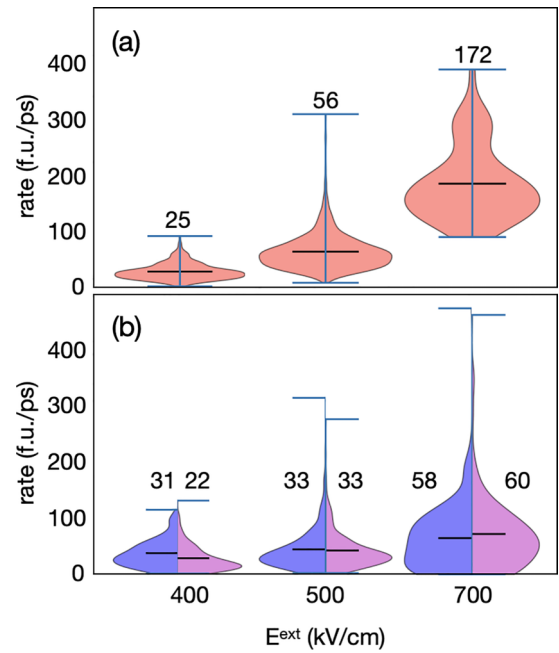

FIG. 6. Distributions of growth rates of clusters of the size estimated in the previous figure for 400, 500, and 700 kV/cm. The distributions are displayed as "violins," where the vertical line centered on the respective field strength value corresponds to a probability of zero. The field-dependent distribution of the blue and magenta clusters is shown left and right of the horizontal "zero line" to allow their statistical comparison in (b). In (a), the distribution for the red is mirrored for visual uniformity. Black horizontal lines mark mean values and the lower and upper "whiskers" extending from the violin plot indicate the minimum and maximum values of the data distribution. Numbers display the median of each distribution in f.u./ps.

initial than for final switching, while the number of persisting clusters is about two times larger for final switching. This shows that thermal fluctuations and nucleation are more relevant for initial switching and both switching steps follow different dynamics. With increasing field strength, the number of initial disappearing clusters is reduced (by a factor of 1.5 for 700 kV/cm) as more clusters form stable nuclei and the number of persisting clusters increases by a factor of about 3.

Figure 5(a) compares the average critical areas, i.e., number of f.u. in a cluster, for different field strengths. The difference between blue and magenta clusters is the error given by the used fitting and the finite number of statistical samples as equal properties of blue and red clusters are expected in the thermodynamic limit. For 400 kV/cm, the critical cluster size for initial switching is approximately 10 f.u. With increasing field strength, field induced fluctuations and this area increase linearly to about 50 f.u. For red clusters, the critical area is larger and increases linearly to about 80 f.u. This is mainly because much fewer smaller clusters are formed by thermal fluctuations, while the area of crossing initial clusters switching to red increases with the field strength.

It is important to note that due to the bound charge formation on the z and y interfaces of blue and magenta clusters, respectively, the initial clusters and their growth are not isotropic. Figure 5(b) shows the dependence of the critical extents on the field strength. Persisting initial clusters show critical extents along the long and short axes in the range of 10 and 3 f.u. In agreement with classical nucleation theory [18], the nuclei are thus elongated along the direction of the switched polarization; however, they show an approximate

rectangular rather than triangular shape. For the red cluster, the difference of the extent is on the level of noise (below 2 f.u.).

Once formed, the growth of the clusters depends on the field strength. Figure 6 shows the distributions of the averaged growth rates in f.u./ps of clusters at critical area for three different values of the field. For each data set, the distribution is shown in a "violin" along the vertical direction, and horizontal lines mark the mean values and minima/maxima of the distribution. For red clusters, the distributions are symmetrically mirrored in violine plots [Fig. 6(a)], while the difference between blue and magenta clusters is compared in the left and right parts of each violin in Fig. 6(b). The median of the initial clusters increases from about 26 f.u./ps at 400 kV/cm to about 33 and 59 f.u./ps at 500 and 700 kV/cm, respectively. Furthermore, increasing the field strength results in the broadening of the distributions, both around the main peak as well as the tail; cf. blue vertical line segments above the violins highlighting each maximum. The red direction shows similar median values at 400 and 500 kV/cm. At 700 kV/cm, its minimal switching rate increases to 90 f.u./ps and a second peak around 300 f.u./ps appears. This again hints to the fact that the final switching in large fields is dominated by the crossing of large initial clusters which switch to red within few time steps.
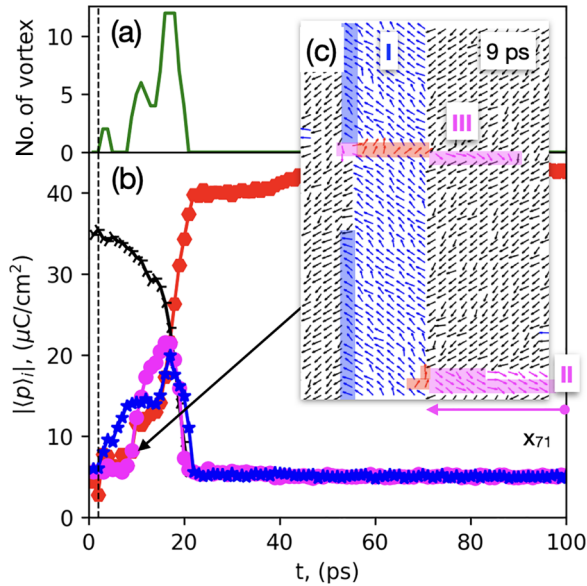
FIG. 7. Exemplarily switching scenarios on the moving DW for 400 kV/cm and slice x_{71}. (a) Time evolution of the number of vortices on that layer. (b) Change of the mean polarization along red, blue, magenta, and black directions. An excerpt of the slice is shown for the time marked by the black arrow. Colors encode the direction of the polarization and the colored background highlights the growth of clusters in the last ps. Three clusters can be distinguished: (I) and (II) blue and magenta clusters nucleated before, as well as (III) magenta or red cluster nucleated within the last ps.

Two typical scenarios of nucleation and initial growth are depicted in the inset of Fig. 7: The light background colors mark the change of the clusters in the last picosecond. Within this short period, the blue (I) and magenta (II) clusters have grown by about 40 and 6 f.u., respectively, and have crossed. Thereby, forward switching from blue to red sets in at the interface. One red cluster, thus, forms by the crossing of two initial clusters, which is the most likely scenario for large field strength, as discussed above. In addition to this scenario, forward switching by the nucleation of a new red cluster (III) may also be possible. However, the time resolution is not sufficient to disentangle this process from the nucleation of and crossing of a new magenta cluster (III).

For both switching scenarios, the mean polarization on the slice follows the trends shown in Fig. 7(b): Either blue, magenta, or both types of clusters nucleate. Due to the depolarization field, these initial clusters commonly span the whole system along the depolarization direction within less than 2 ps,[4] i.e., with a speed of approximately 4700 m/s close to the velocity of sound in the material for all field strengths [56]. For the switching behavior of a single cluster within a slice, this means that a cluster with an initial extent of 3 f.u. covers the whole slice length within 2 ps. After that, the different regions on the wall are separated by one-dimensional O90 walls running along [010] and [001] with a typical width of less than 2 f.u. These one-dimensional walls exhibit a slower sideways motion. Thus, each wall splits into

two-dimensional regions with either black and red interfaces (Ising-type wall) or intermediate blue or magenta polarization (Bloch-type wall). In this transient state, polarization vortices form at the boundaries between the different type of clusters. The number of vortices is always maximal if the domain wall is centered on a particular layer; cf. Fig. 7(a). However, as soon as the domain wall has passed the slice or if the field is switched off, the vortices disappear. The final switching is fast since the entire crossings of both domain types switch at once. At this stage, we typically observe that several initial clusters have already nucleated, which results in faster switching by merging. With increasing field strength, the probabilities for initial nucleation as well as for merging and crossing of cluster increase, which results in the previously discussed increase of the domain wall speed.

B. Generalization to other domain walls

Why is the discussed 90° rotation of the polarization of a fraction of dipoles possible and favorable on the wall? Because of the large electromechanical coupling, this observation is unexpected. What are the properties of the O180 walls that allow the discussed multistep switching and is this scenario possible with other types of DWs?

First, one may expect that the multistep switching by nucleation and growth is favorable if the transient state is low in energy. Indeed, the blue and magenta polarization directions are metastable orthorhombic states. Clusters with these polarization directions as well as the black initial state share elastically and electrically compatible O90 walls which are low in energy [24] as well as stable down to few unit cells [57]. Second, the answer might be hidden in the bound charge that forms if a local dipole switches the sign of polarization component *i*. In the case of 90° switching, all dipoles change only one polarization component, thereby reducing the bound charge by a factor of about two compared to the full 180° switching. Third, one may expect a large probability for nucleation by thermal fluctuations if either one polarization component switches or two highly correlated components switch at the same time. On the other hand, the instantaneous switching of two uncorrelated components is rather unlikely. As discussed above, only one component switches on the moving O180 wall. Fourth, the energy barrier for direct switching needs to be higher than the energy barriers for the multiple switching events. Since the free energy of the orthorhombic phase is closer to the tetragonal phase (barriers for the switching of one component) than to the cubic phase (barrier for switching via zero polarization), this is indeed true for the O180 wall.

To test these hypotheses, we compare our results for the O180 wall to one example without multistep switching (T180) and one example with multistep switching (R109) walls. On the one hand, multistep switching by 90° would be possible on the moving T180 wall via a transient T90 state. However, for such switching, two polarization components have to switch at the same time and these DWs would induce an elastic distortion, i.e., are higher in energy and cover a larger volume. Furthermore, the difference of free energies between paraelectric and tetragonal phases is smaller than between paraelectric and orthorhombic phases and thus also
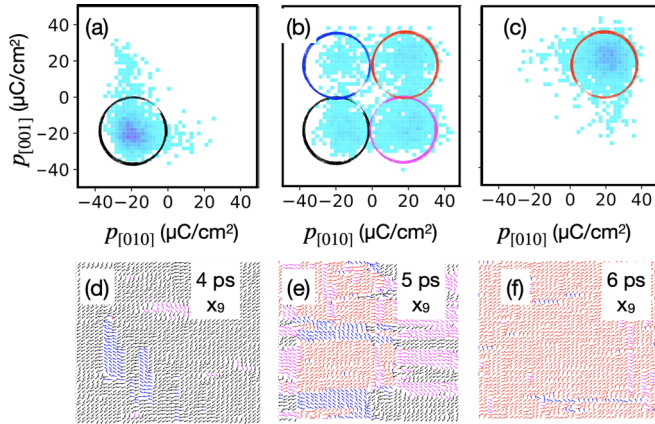
---

[4]Verified for 10 checked samples.

FIG. 8. Rhombohedral phase with initial R109 walls at 50 K after a field of 300 kV/cm has been applied along [111]. Time evolution of the dipole distribution on slice x_9 (a)–(c) in $p_{[010]} - p_{[001]}$ space and (d)–(f) in real space. Colors encode (a)–(c) the number of dipoles per $(2.06 \, \mu C/cm^2)^2$ area or (d)–(f) the sign of the [010] and [001] components of polarization. Note that the distribution of p_x is approximately constant with time.

the energy barrier for direct Ising-type switching is probably smaller compared to the O180 wall. Indeed, and in agreement with Refs. [11,16], we rather observe domain wall motion by single-step local switching, nucleation, and growth of clusters; see the Appendix. Thereby, the dipole distribution along the perpendicular directions is broad with and without DWs or fields.

As a second example, we pick R109 walls, which can be understood as O180 with an additional homogeneous polarization along x. Here, one may expect transient $[11\bar{1}]$ and $[1\bar{1}1]$ domains after switching of one polarization components. In the R phase, one may furthermore expect an even larger energy barrier to switch via the paraelectric state without polarization. Results for the R phase are collected in Fig. 8. Indeed, for a field of 300 kV/cm, we observe the nucleation and growth of $[11\bar{1}]$ and $[1\bar{1}1]$ domains on the wall with similar trends for the distribution of dipoles as for O180 walls. We thus can reproduce the predictions by Landau theory that Bloch-like R109 walls are possible and that they can be interpreted as two coupled $71°$ DWs [28]. In agreement with the O phase, furthermore, a fast bulklike switching can be activated for larger fields; cf. Sec. III C. Note that for the R phase, both the polarization and the applied field have a component along the wall normal and the high-field switching can already be activated for 300 kV/cm. In the shown example, the switching is dominated by domain wall motion. However the dipole distribution in the first ps (not shown) shows signs of monoclinic distortions with spatial correlation after the instantaneous field application. After 4 ps, the system already relaxed back from this nonequilibrium state, analogous to the discussion in Ref. [39]. However, the initial nucleations of blue and magenta clusters show a corresponding spatial preference.

C. High-field switching

In this section, we discuss bulklike switching in the field regime III which can be activated by high fields in the or-
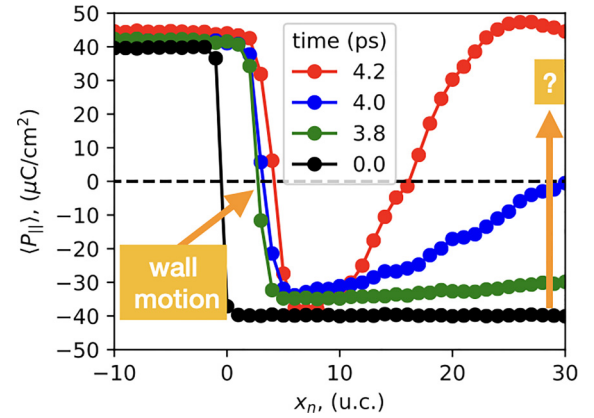

FIG. 9. Change of the polarization profile for high-field switching: While the O180 domain wall initially centered at $x = 0$ moves through the system, a faster polarization rotation sets in at the center of the black domain.

thorhombic phase. As shown in Fig. 9, this switching is related to the rise of $P_{\parallel}$ in the center of the black domain, e.g., for the given example layers with $P_{\parallel} = 0$ and positive saturation polarization exist well apart from the traveling initial domain wall after about 4 ps and 4.2 ps, correspondingly. Note that homogeneous nucleation and fast switching in the center of the domain have also been reported for the tetragonal phase [11].

Figures 10(a)–10(f) exemplify the underlying microscopic processes in the O phase for one layer being initially in the center of the black domain for an independent simulation run. In contrast to the local nucleation and growth of blue and magenta clusters relevant for wall motion, the polarization on the whole slice breaks into two types of domains separated by equidistant walls along $[0\bar{1}1]$.[5] In these domains, the polarization switches approximately uniformly by continuous polarization rotation. The system shows a spatially correlated switching. For instance, after 4.1 ps, most of the dipoles can still be classified as black; however, the polarization does not point along $[0\bar{1}\bar{1}]$, but rather scatters around $[0\bar{1}0]$ and $[00\bar{1}]$ in the domains marked by green and orange arrows, respectively. Thus the layer is locally in a distorted T90 domain structure. Already after 4.3 ps, the local polarization rotates towards $\pm[0\bar{1}1]$ with O180 walls along $[0\bar{1}1]$ and, finally, the single-domain red state is reached via an intermediate T90 configuration with [010] and [001] domains.

Why does this homogeneous rotation of the polarization not induce large electric and elastic energy penalties? First of all, there is no depolarization field, as both the intermediate T90 and the O180 domain structures are charge neutral. Second, the domains are elastically compatible, minimizing the elastic energy on the plane [24]. Third, the macroscopic strain relative to the surrounding black matrix is minimized as polarization and strain rotation in both domains are fully symmetric. The latter can be clearly seen in the dipole distribution in $p_y - p_z$ space shown in Figs. 10(g)–10(l): After

---

[5]We always find four domain walls in our simulation, which is the minimal number of walls along ⟨110⟩-type directions to fulfill periodic boundary conditions.
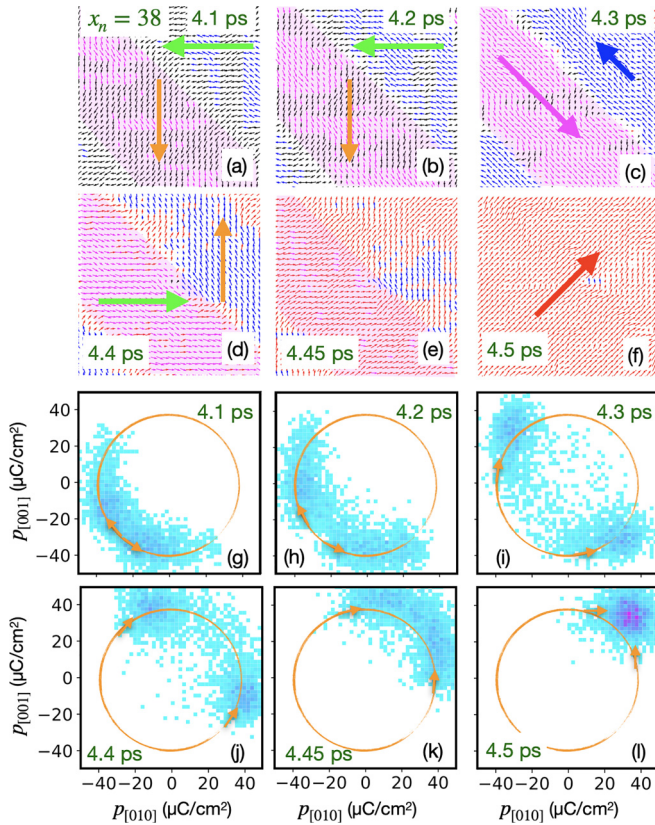
FIG. 10. Time evolution of the dipole distribution on the orthorhombic phase in slice x_{38} for the bulklike switching in field regime III after 700 kV/cm have been applied along the red direction (a)–(f) real space: Excerpt of the local dipoles colored via their classes. The magenta background marks the newly formed two-dimensional domains. Large arrows highlight their macroscopic polarization directions. Blue: $[0\bar{1}1]$; magenta: $[01\bar{1}]$; orange: $\pm[001]$; and green: $\pm[010]$ (g)–(l) $p[010] - -p[001]$ space: Colors encode the number of dipoles per $(2.06 \, \mu C/cm^2)^2$ area and the orange arrowheads highlight the continuous rotation path of the maxima of the distributions of both domains.

4.1 ps, two distinct maxima of the distribution have formed and rotate clockwise and counterclockwise towards the final single-domain state. Thus, a decrease of polarization and strain along [010] in the orange domain is fully compensated by the corresponding increase of the green domain with equal area. However, as T90 walls are higher in energy than O90 ones, particularly in the temperature range of the O phase, this intermediate state can only be activated by high field strengths.

Excitingly, the observed switching process in both domains is quasicontinuous, and thus in contrast to the commonly accepted picture of discrete ferroelectric switching. Although the dipole distribution shows clear maxima at each time step, these maxima rotate approximately continuously on the shown orange sphere and all intermediate states are populated; cf. the large weight of the distributions on the rotation path. For the intermediate O180 state (4.3 ps), furthermore, some dipoles also populate the center of the plane. However, note that this does not correspond to direct 180° switching as the initial state is no longer existing in the excited material.

During the switching process, the complex three-dimensional nucleus gradually expands towards the DWs and, once it reaches a moving wall, the whole switching is dominated by the three-dimensional (3D) polarization rotation. The faster switching can be related to continuous 3D switching in a large volume fraction vs discrete nucleation events followed by mainly 2D growth of nuclei for the domain wall motion in regime (II).

IV. CONCLUSION

We have used molecular dynamics simulations to study the underlying microscopic processes of field induced switching of the orthorhombic phase of $BaTiO_3$. For moderate field strengths, we have shown that switching is dominated by two-dimensional nucleation and growth in front of traveling O180 domain walls. In contrast to the direct 180° switching on the well-studied tetragonal walls, the O180 walls show a local realization of multistep 90° switching. In their transient state, the moving walls split into two-dimensional domains which are separated by one-dimensional O90 walls and polarization vortices and host Ising-type and Bloch-type regions.

We have analyzed the time evolution of this switching process and showed that the domain wall motion is dominated by a thermally activated nucleation of clusters with 90° polarization relative to the applied field. The size, width, probability of appearance of critical clusters, and their growth rates increase with the field strength. This results in the expected increase of the domain wall velocity with field strength. The final switching step follows different dynamics and is often related to the crossing of existing clusters rather than nucleation. It is, thus, promising to control the dynamics of the domain walls by means of tailoring the local energy barriers for 90° switching, for example e.g., by defects, inhomogeneities, or straining.

We were able to relate the multistep switching to the low energy of the transient state on the O180 wall and the larger probability to switch one component of the polarization. These results can be transferred to other types of domain walls and a similar multistep switching is possible for R109° walls.

For large fields, we have shown that a second ultrafast multistep switching channel can be activated. Thereby, homogeneous and uniform polarization rotation via an intermediate tetragonal 90° domain structure sets in at the middle of the domain and the three-dimensional nucleus expands through the whole system in the span of a few picoseconds. We thus observed a quasicontinuous switching process, which may shed light on the understanding of microscopic dipole switching and boost the development of conceptually new switching models.

Scripts for the data analysis are openly available in our repository [53]. The library we used to analyze and characterize clusters is openly available in a second git repository [58]. Original raw data can be provided by the authors upon reasonable request.
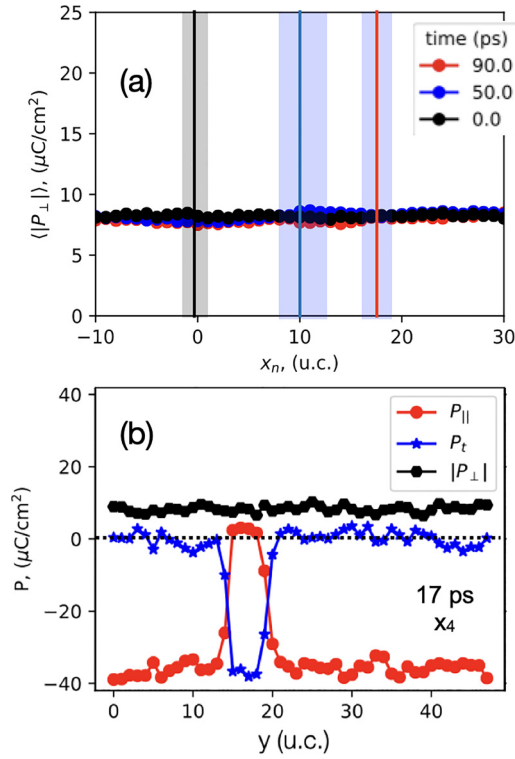
FIG. 11. Change of the spatial distribution of dipoles with time, after 500 kV/cm have been applied. (a) Polarization profile $P_\perp$, i.e., the polarization projection on [100], across the O180 domain wall (black) and its time evolution after an external field of $E^{\mathrm{ext}} = 500$ kV/cm has been applied along [011] after 90 ps (red) and 50 ps (blue) (cf. Fig. 3). Note that the sign of the projection has been removed before averaging. Vertical lines and shaded areas highlight the center and the width of the domain wall at the corresponding time step. (b) Mean polarization along [010] averaged over [001] planes on x_4 shown in Fig. 4. Indeed, there is no Néel-like polarization component either locally or globally and there is a sharp 90° domain wall.

APPENDIX

In this Appendix, we present additional figures. Figure 11(a) shows the absence of Néel polarization rotation across the moving orthorhombic domain walls at 0 ps (black),
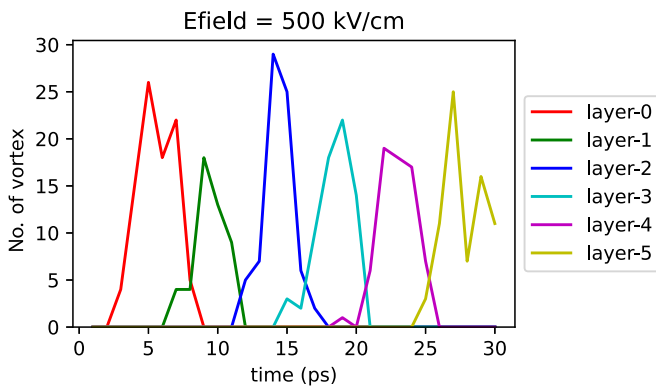

FIG. 12. Time evolution of the number of vortices on layers (slices) x with an interface area of about 360 nm^2 after 500 kV/cm have been applied.
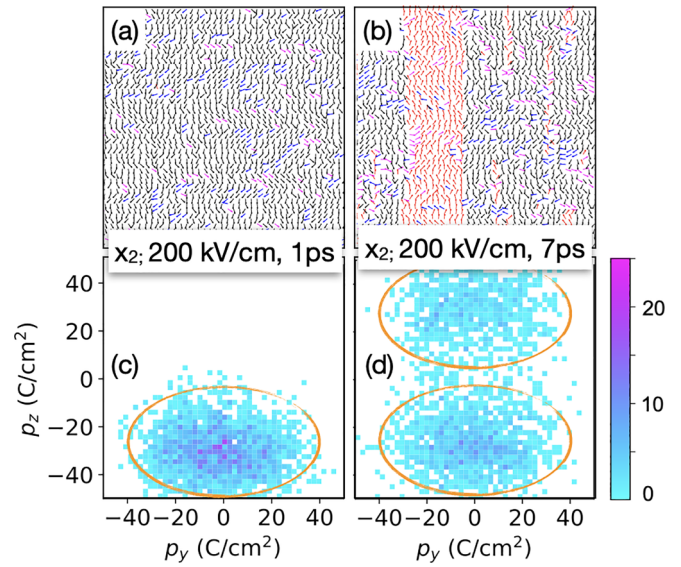

FIG. 13. Change of the (a),(b) spatial and (c)–(e) statistical distribution of dipoles with time (a),(c) 1 ps and (b),(e) 7 ps, after a field has been applied along [001] to the tetragonal domain structure with [001] (red) and [00$\bar{1}$] (black) domains at 240 K.

50 ps (blue), and 90 ps (red) after an external field of 500 kV/cm has been applied for the same configuration shown in Fig. 11. Vertical lines mark the corresponding position of the domain wall centers. In Fig. 11(b), all three polarization components $P_{||}$, P_t, and $P_\perp$ are shown across a one-dimensional domain wall centered at about 18 f.u. Also locally on that wall, no enhanced Néel-like polarization rotation exit.

Figure 12 compares the time evolution of the number of vortices on different layers for the example of an external field of 500 kV/cm. For all layers, this number is maximal if the wall crosses them.

Figure 13 shows the time evolution of the local polarization in the presence of a moving tetragonal 180° wall. In Figs. 13(a) and 13(c), the domain wall has not reached the layer 2 and the dipoles scatter in a broad range of p_y values around the tetragonal state with finite P_z. In Figs. 13(b) and 13(d), the wall reached the plane and dipoles in a two-dimensional area have switched by 180°. The dipole distribution now scatters around both tetragonal states with $\pm P_z$.
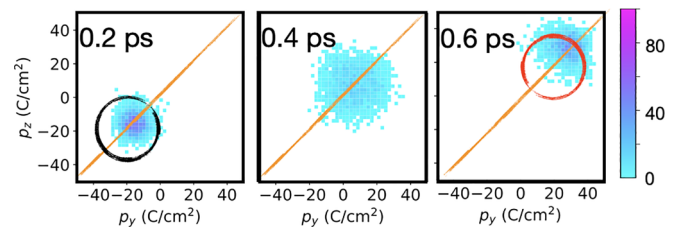

FIG. 14. Single-step high-field switching of the rhombohedral phase (50 K): Change of the dipole distribution during field induced wall motion (a)–(c) $p_y - p_z$ space on slice $x_n = 30$ after an external field of 400 kV/cm has been applied along [111]. Colors encode the number of dipoles per $(2.06\,\mu C/cm^2)^2$ area. Note that the distribution of p_x is approximately constant with time.

In Fig. 14, the time evolution of the dipole distribution of the rhombohedral phase in the high-field regime is shown. The polarization switches quickly via the state with $P_y = P_z = 0$.

[1] K. Nakayama, Y. Miyata, G. N. Phan, T. Sato, Y. Tanabe, T. Urata, K. Tanigaki, and T. Takahashi, Phys. Rev. Lett. **113**, 237001 (2014).

[2] J. E. Daniels, C. Cozzan, S. Ukritnukun, G. Tutuncu, J. Andrieux, J. Glaum, C. Dosch, W. Jo, and J. L. Jones, J. Appl. Phys. **115**, 224104 (2014).

[3] Y. A. Genenko, R. Khachaturyan, J. Schultheiß, A. Ossipov, J. E. Daniels, and J. Koruza, Phys. Rev. B **97**, 144101 (2018).

[4] Y. A. Genenko, R. Khachaturyan, I. S. Vorotiahin, J. Schultheiß, J. E. Daniels, A. Grünebohm, and J. Koruza, Phys. Rev. B **102**, 064107 (2020).

[5] H.-Y. Huang, M. Wu, and L.-J. Qiao, Comput. Mater. Sci. **82**, 1 (2014).

[6] B. Jiang, Y. Bai, W. Chu, Y. Su, and L. Qiao, Appl. Phys. Lett. **93**, 152905 (2008).

[7] C.-L. Jia, K. W. Urban, M. Alexe, D. Hesse, and I. Vrejoiu, Science **331**, 1420 (2011).

[8] D. Zhu, X. Cheng, C. Yang, L. Shui, and Y. Li, Mater. Lett. **282**, 128706 (2021).

[9] C. Fancher, S. Brewer, C. Chung, S. Röhrig, T. Rojac, G. Esteves, M. Deluca, N. Bassiri-Gharb, and J. Jones, Acta Mater. **126**, 36 (2017).

[10] J. Schultheiß, L. Liu, H. Kungl, M. Weber, L. Kodumudi Venkataraman, S. Checchia, D. Damjanovic, J. E. Daniels, and J. Koruza, Acta Mater. **157**, 355 (2018).

[11] V. Boddu, F. Endres, and P. Steinmann, Sci. Rep. **7**, 806 (2017).

[12] W. J. Merz, Phys. Rev. **95**, 690 (1954).

[13] A.-Q. Jiang, H. J. Lee, C. S. Hwang, and T.-A. Tang, Phys. Rev. B **80**, 024119 (2009).

[14] A. Grünebohm, M. Marathe, R. Khachaturyan, R. Schiedung, D. C. Lupascu, and V. V. Shvartsman, J. Phys. Cond. Matter **34**, 073002 (2022).

[15] Y.-H. Shin, I. Grinberg, I.-W. Chen, and A. M. Rappe, Nature (London) **449**, 881 (2007).

[16] A. J. Klomp, R. Khachaturyan, T. Wallis, K. Albe, and A. Grünebohm, Phys. Rev. Mater. **6**, 104411 (2022).

[17] V. Ya. Shur and P. S. Zelenovskiy, J. Appl. Phys. **116**, 066802 (2014).

[18] A. Tagantsev, L. E. Cross, and J. Fousek, *Domains in Ferroic Crystals and Thin Films* (Springer-Verlag, New York, 2010).

[19] R. C. Miller and G. Weinreich, Phys. Rev. **117**, 1460 (1960).

[20] J. Schultheiß, G. Picht, J. Wang, Y. A. Genenko, L. Q. Chen, J. E. Daniels, and J. Koruza, Prog. Mater. Sci. **136**, 101101 (2023).

[21] G. F. Nataf, M. Guennou, J. M. Gregg, D. Meier, J. Hlinka, E. K. H. Salje, and J. Kreisel, Nat. Rev. Phys. **2**, 634 (2020).

[22] P. V. Yudin, A. K. Tagantsev, and N. Setter, Ferroelectrics **438**, 20 (2012).

[23] X. R. Huang, S. S. Jiang, X. B. Hu, and W. J. Liu, J. Phys.: Condens. Matter **9**, 4467 (1997).

[24] P. Marton, I. Rychetsky, and J. Hlinka, Phys. Rev. B **81**, 144125 (2010).

[25] V. Stepkova, P. Marton, and J. Hlinka, Phys. Rev. B **92**, 094106 (2015).

[26] J. Hlinka, V. Stepkova, P. Marton, I. Rychetsky, V. Janovec, and P. Ondrejkovic, Phase Transitions **84**, 738 (2011).

[27] V. Stepkova, P. Marton, and J. Hlinka, J. Phys.: Condens. Matter **24**, 212201 (2012).

[28] M. Taherinejad, D. Vanderbilt, P. Marton, V. Stepkova, and J. Hlinka, Phys. Rev. B **86**, 155138 (2012).

[29] S. Cherifi-Hertel, C. Voulot, U. Acevedo-Salas, Y. Zhang, O. Crégut, K. D. Dorkenoo, and R. Hertel, J. Appl. Phys. **129**, 081101 (2021).

[30] Y. J. Wang, D. Chen, Y. L. Tang, Y. L. Zhu, and X. L. Ma, J. Appl. Phys. **116**, 224105 (2014).

[31] J. C. Wojdeł and J. Íñiguez, Phys. Rev. Lett. **112**, 247603 (2014).

[32] P. V. Yudin, A. K. Tagantsev, E. A. Eliseev, A. N. Morozovska, and N. Setter, Phys. Rev. B **86**, 134102 (2012).

[33] Y. Gu, M. Li, A. N. Morozovska, Y. Wang, E. A. Eliseev, V. Gopalan, and L.-Q. Chen, Phys. Rev. B **89**, 174111 (2014).

[34] M. Li, Y. Gu, Y. Wang, L.-Q. Chen, and W. Duan, Phys. Rev. B **90**, 054106 (2014).

[35] F. Zavaliche, P. Shafer, R. Ramesh, M. P. Cruz, R. R. Das, D. M. Kim, and C. B. Eom, Appl. Phys. Lett. **87**, 252902 (2005).

[36] S. Cherifi-Hertel, H. Bulou, R. Hertel, G. Taupier, K. D. Dorkenoo, C. Andreas, J. Guyonnet, I. Gaponenko, K. Gallo, and P. Paruch, Nat. Commun. **8**, 15768 (2017).

[37] N. Balke, B. Winchester, W. Ren, A. N. Chu, Ying Hao Morozovska, E. A. Eliseev, M. Huijben, R. K. Vasudevan, P. Maksymovych, J. Britson, S. Jesse *et al.*, Nat. Phys. **8**, 81 (2012).

[38] Z. Hong, S. Das, C. Nelson, A. Yadav, Y. Wu, J. Junquera, L.-Q. Chen, L. W. Martin, and R. Ramesh, Nano Lett. **21**, 3533 (2021).

[39] R. Khachaturyan, A. Dimou, and A. Grünebohm, Phys. Status Solidi - Rapid Res. Lett. **16**, 2200038 (2022).

[40] M. Sepliarsky, S. R. Phillpot, S. K. Streiffer, M. G. Stachiotti, and R. L. Migoni, Appl. Phys. Lett. **79**, 4417 (2001).

[41] R. Xu, S. Liu, I. Grinberg, J. Karthik, A. R. Damodaran, A. M. Rappe, and L. W. Martin, Nat. Mater. **14**, 79 (2015).

[42] J. Paul, T. Nishimatsu, Y. Kawazoe, and U. V. Waghmare, Phys. Rev. B **80**, 024107 (2009).

[43] W. Zhong, D. Vanderbilt, and K. M. Rabe, Phys. Rev. B **52**, 6301 (1995).

[44] T. Nishimatsu, M. Iwamoto, Y. Kawazoe, and U. V. Waghmare, Phys. Rev. B **82**, 134106 (2010).

[45] T. Nishimatsu, U. V. Waghmare, Y. Kawazoe, and D. Vanderbilt, Phys. Rev. B **78**, 104104 (2008).

[46] B.-K. Lai, I. Ponomareva, I. A. Kornev, L. Bellaiche, and G. J. Salamo, Phys. Rev. B **75**, 085412 (2007).

[47] A. Grünebohm, M. Marathe, and C. Ederer, Appl. Phys. Lett. **107**, 102901 (2015).

[48] E. Soergel, Appl. Phys. B **81**, 729 (2005).

[49] A. Gruenebohm, M. E. Gruner, and P. Entel, Ferroelectrics **426**, 21 (2012).

[50] S. D. Bond, B. J. Leimkuhler, and B. B. Laird, J. Comput. Phys. **151**, 114 (1999).

[51] X. Tricoche, G. Scheuermann, and H. Hagen, in *Proceedings in Visualization, 2001, VIS '01, San Diego, CA, USA* (IEEE, Piscataway, NJ, 2001), pp. 159–166.

[52] S. van der Walt, J. L. Schönberger, J. Nunez-Iglesias, F. Boulogne, J. D. Warner, N. Yager, E. Gouillart, T. Yu, and the scikit-image contributors, PeerJ **2**, e453 (2014).

[53] R. K. Sheng-Han Teng, Benjamin Udofia and M. Stricker, Jupyter notebooks related to this publication are collected in the SCF GIT repository (2023), https://gitlab.ruhr-uni-bochum.de/icams-sfc/ortho_2023.

[54] J. Očenášek, J. Minár, and J. Alcalá, npj Comput. Mater. **9**, 118 (2023).

[55] Y. A. Genenko, M.-H. Zhang, I. S. Vorotiahin, R. Khachaturyan, Y.-X. Liu, J.-W. Li, K. Wang, and J. Koruza, Phys. Rev. B **104**, 184106 (2021).

[56] J. W. Lee, J.-H. Ko, K. Roleder, and D. Rytz, J. Korean Phys. Soc. **74**, 1089 (2019).

[57] A. Grünebohm and M. Marathe, Phys. Rev. Mater. **4**, 114417 (2020).

[58] B. U. Markus Stricker, Ferrowallnucleation Library (2022), git@gitlab.ruhr-uni-bochum.de:stricm9y/ferrowallnucleation.git.